JOURNAL OF APPLIED CRYSTALLOGRAPHY

ISSN 1600-5767

Anisotropy factors in small-angle scattering for dilute rigid-rod suspensions

Jack Rooks,[a,b] Peter H. Gilbert,[b,c]*‡ Lionel Porcar,[d] Yun Liu[b,c]* and Paul Butler[b,c]

[a]Department of Chemical and Biological Engineering, University at Buffalo, State University of New York, Buffalo, NY 14260, USA, [b]Department of Chemical and Biomolecular Engineering, Center for Neutron Science, University of Delaware, Newark, DE 19716, USA, [c]NIST Center for Neutron Research, National Institute of Standards and Technology, Gaithersburg, MD 20899, USA, and [d]Institut Laue–Langevin, Grenoble, France. *Correspondence e-mail: peter.gilbert@queensu.ca, yun.liu@nist.gov

Received 12 July 2022
Accepted 7 March 2023

Edited by G. J. McIntyre, Australian Nuclear Science and Technology Organisation, Lucas Heights, Australia

‡ Present address: Department of Chemical Engineering, Queen's University, Kingston, ON K7L 3N6, Canada.

Keywords: small-angle neutron scattering; anisotropy factors; alignment; wormlike micelles; anisotropy; small-angle scattering.

Supporting information: this article has supporting information at journals.iucr.org/j

Alignment of anisotropic particles along specific orientations influences the mechanical and rheological properties of a material. Small-angle scattering techniques are widely used to probe this alignment through analysis of anisotropic two-dimensional scattering intensity patterns. The anisotropy factor is the simplest and most common quantitative parameter for describing scattering anisotropy, especially in systems containing rod-like particles, and there are several methods for calculating this factor. However, there has been no systematic study comparing these methods while also evaluating the limitations imposed by non-idealities from instrumentation or polydisperse morphology. Three of the most common methods for calculating an anisotropy factor are examined here and their effectiveness for describing the orientation of a theoretical cylinder is evaluated. It is found that the maximum theoretical value of 1 for the anisotropy factor is only accessible at certain values of scattering vector q. The analysis details recommendations for q-range selection and data binning, as these influence the calculations. The theoretical results are supported by experimental small-angle neutron scattering data for a wormlike micelle solution undergoing shear, where different calculation methods yield distinct quantifications of anisotropy.

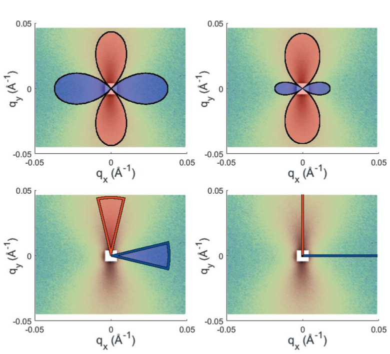

1. Introduction

Small-angle scattering (SAS) techniques are commonly used to characterize the morphology and orientation of macromolecules using two-dimensional scattering patterns (Jeffries *et al.*, 2021; Schmidt *et al.*, 2002; Hongladarom *et al.*, 1996;Salem & Fuller, 1985). Solutions containing randomly oriented or unoriented particles produce isotropic scattering intensity patterns that are circularly symmetric about the beam center (light, X-rays or neutrons) (Schmidt *et al.*, 2002). When these particles become oriented or aligned with an external field (*e.g.* a flow, electric, magnetic or temperature gradient), the 2D scattering pattern becomes anisotropic or asymmetric (Schmidt *et al.*, 2002; Hongladarom *et al.*, 1996; Walker & Wagner, 1996; Lacková *et al.*, 2021). Methods have recently been developed to estimate the 3D particle orientation distribution from SAS measurements, connecting scattering patterns to particle orientation and material properties (Corona *et al.*, 2021; Wang *et al.*, 2017). These methods are extremely useful in understanding comprehensively the connection between scattering anisotropy and particle orientation, but they are relatively complicated to implement. X-ray cross-correlation analysis (XCCA) can also reveal local ordering and folding symmetry of hard-particle solutions by applying an angular autocorrelation function to the 2D scattering pattern (Markmann *et al.*, 2020; Zaluzhnyy *et al.*, 2019). This method yields valuable new information on orientation and particle ordering by assuming a relationship between scattering anisotropy and the orientation distribution. XCCA requires highly resolved 2D scattering patterns that may be achieved with X-ray scattering but could be challenging for small-angle neutron scattering (Kurta *et al.*, 2019).

A simpler parameter, traditionally called the alignment factor or $A_{\rm f}$, is commonly used to quantify scattering anisotropy in favor of more complicated analyses. In this work, the term *alignment factor* is replaced by *anisotropy factor*, as these quantities are calculated from scattering anisotropy and are not directly linked to particle alignment or orientation. This use of anisotropy language has already been adopted for similar analyses in SAXS (Pujari *et al.*, 2011).

The anisotropy factor $A_{\rm f}$ is the simplest parameter for quantifying 2D scattering anisotropy, which can be caused by particle and macromolecular orientation relative to the incident beam. $A_{\rm f}$ typically ranges from 0 for isotropic scattering to 1 for an anisotropic line of intensity. Negative anisotropy factors can arise from alignment perpendicular to the reference scattering angle (*e.g.* flow direction), sometimes called the director (Walker & Wagner, 1996; Walker, 1995; Liberatore *et al.*, 2009). Although anisotropy factors calculated by any method range from 0 to 1 (excluding negative values), each method can report a different value for a single anisotropic scattering pattern. It is also unclear how values of the anisotropy factor between 0 and 1 correlate with particle alignment. Thus, anisotropy factors are used exclusively in a qualitative fashion by characterizing changes in alignment-dependent scattering anisotropy within a single system (*e.g.* changing particle alignment with shear rate) (Walker & Wagner, 1996; Wade *et al.*, 2020; Hayward *et al.*, 2021). Great care must be taken when comparing anisotropy factors for different orientable particles.

Several mathematical methods have been developed for calculating the anisotropy factor. Each method arises from a unique historical context and may not share the same assumptions and justification as its sister methods. Thus, examination of each calculation method is necessary to gain a full understanding of anisotropy factor usage in the literature. The three anisotropy factor calculation methods considered here will be referred to as the cosine expansion (Hongladarom *et al.*, 1996; Walker & Wagner, 1996; Wang *et al.*, 2017), the Legendre expansion (sometimes called the order parameter) (Kurta *et al.*, 2019; Maier & Saupe, 1959; Chatelain, 1955) and axial integration (Iwase *et al.*, 2019; Andriano *et al.*, 2020; Gazeau *et al.*, 2002). The equations used to calculate the anisotropy factor with each of these methods are detailed in Section 2.6. The discussed methods are alternative definitions of the anisotropy factor offered by the SAS community and only characterize the amount of anisotropic scattering. These methods neither depend on nor are specific to particle morphology and orientation.

The cosine expansion first appears as equation (3) of Walker & Wagner (1996), where alignment in a wormlike micelle (WLM) solution was examined. Walker produced an anisotropy factor that weighted 2D scattering intensity data with a cosine expansion of even harmonics curtailed at the second term [see equation 5.30 of Wang *et al.* (2017)], $\cos 2\phi_{\rm s}$, where $\phi_{\rm s}$ is the azimuthal scattering angle in Fig. 1. This initial function was later modified in work from the Wagner group (Walker & Wagner, 1996) and the Rogers group (Wade *et al.*, 2020) to include a reference angle $\phi_{\rm s,0}$ defining the angle of the principal scattering axis which is perpendicular to the particle orientation axis. This allows the orientation to be evaluated along any axis, beyond horizontal and vertical. This cosine expansion method continues to enjoy broad usage in the small-angle neutron scattering (SANS) community (Corona *et al.*, 2018; Wade *et al.*, 2020; Muthig *et al.*, 2013).

The Legendre expansion is the oldest method for calculating anisotropy factor and originates from a similar estimate

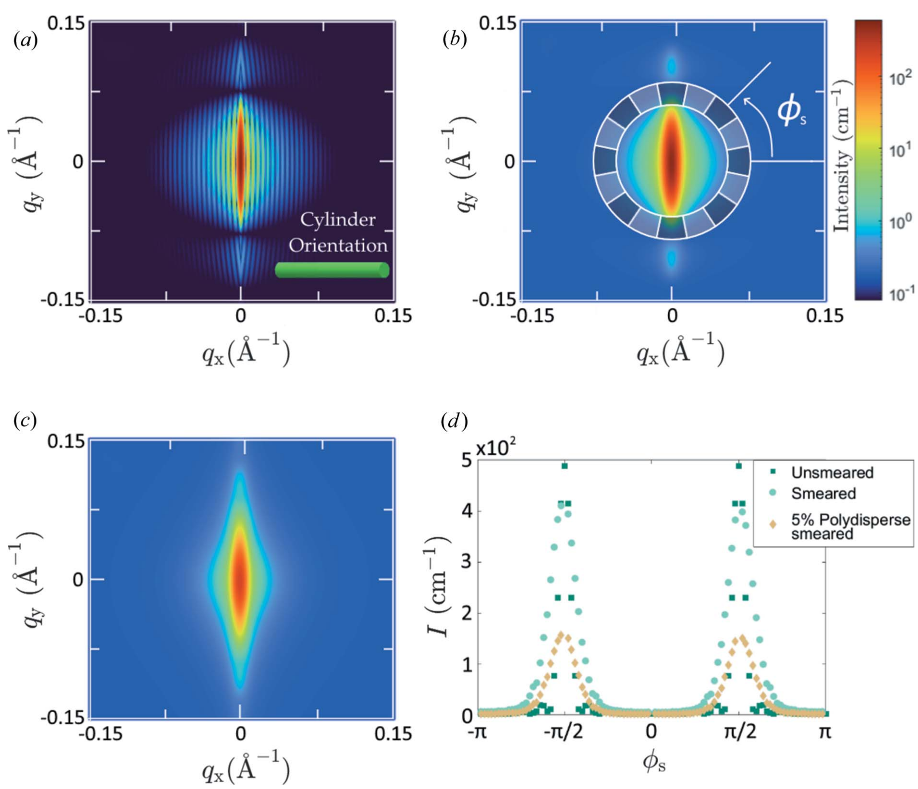

Figure 1
Theoretical 2D scattering intensity patterns for flow-aligned cylinders of length 1800 Å and radius 20 Å corresponding to (*a*) unsmeared scattering with monodisperse cylinders, (*b*) smeared scattering with monodisperse cylinders and (*c*) smeared scattering with 5% radially polydisperse cylinders. (*d*) Scattering intensity $I(\phi_{\rm s})$ versus azimuthal scattering angle $\phi_{\rm s}$ for the theoretical 2D patterns in panels (*a*)–(*c*) for $0.015 \le q \le 0.02$ Å^{-1}. The color bar in panel (*b*) corresponds to $I(q)$ in units of cm^{-1}. Error bars represent one standard deviation and are smaller than the symbols in panel (*d*).

of particle orientation called the order parameter (Chatelain, 1955). Anisotropy factors calculated using this method are often referred to as order parameters or orientation parameters in an interchangeable way (Hongladarom *et al.*, 1996; Kurta *et al.*, 2019). As with the cosine expansion, the Legendre expansion method uses the second-order Legendre polynomial, $P_2(\cos\phi_s) = \frac{1}{2}(3\cos^2\phi_s - 1)$, as a weighting function for the scattering pattern. Legendre expansion anisotropy factors are common throughout the SANS community but are particularly popular for analysis of liquid crystals (Hongladarom *et al.*, 1996; Kurta *et al.*, 2019; Haase *et al.*, 1988). In both expansion methods, A_f is estimated using intensity data within an annular region corresponding to the range in target scattering vector $\mathbf{q}$. Thus, A_f only depends on the q-range selection for a single scattering intensity pattern.

The integrated axes method is the third approach examined in this work and is a modern take on the anisotropy factor (Liberatore *et al.*, 2009; Wade *et al.*, 2020; Hayward *et al.*, 2021). This method requires direct integration of the scattering intensity along each axis of the scattering pattern, vertical and horizontal, for a specified q range. A sector average is taken to include sufficient data for integration along the axes, where a wedge of intensity data within $\phi_{\rm sect} = \pm 2.5^\circ$ (Andriano *et al.*, 2020) to $\phi_{\rm sect} = \pm 15^\circ$ (Iwase *et al.*, 2019; Gazeau *et al.*, 2002) of each axis is averaged. $\phi_{\rm sect}$ is the angle between the edge of the sector and the axis, while $\Delta\phi_{\rm sect}$ is the total sector width, so that $\Delta\phi_{\rm sect} \equiv 2|\phi_{\rm sect}|$. The integrated axes method relies on data within the annular sector bounded by the q range of interest and the selected sector angle.

This work provides a starting point for practitioners to determine which anisotropy factor calculation method is most useful to their research, and it details how each method should be implemented for easier comparison with the literature. The paper aims to clarify the effect of calculation method on estimates of anisotropy factor for an oriented system and evaluates the limitations of these methods. Restrictions imposed by real instrumentation through detector grid spacing (nearest neighbor) and resolution are examined, along with the effect of bin count and selected q range during annular averaging. Guidelines are suggested for extracting a representative anisotropy factor from scattering data. Anisotropy factor analysis on theoretically generated data for oriented cylinders is used to explain our findings. As theoretical cylinders can be perfectly aligned, an anisotropy factor of 1 should be achievable. When perfectly aligned particles are tilted relative to the incident beam or the director angle, the anisotropy factor decreases. Tilt is briefly examined here so that practitioners have some guidance on how to select and analyze data that contain bodies oriented at any angle. Some of the details behind and surrounding anisotropy factor analysis have been placed in the supporting information to simplify discussion; advanced practitioners may find the supporting information useful for more deeply understanding anisotropy factors.

To complete this study, we performed anisotropy factor calculations on experimental SANS data for a flowing WLM solution of 0.03 mol l^{-1} cetrimonium bromide (CTAB) and 0.24 mol l^{-1} sodium salicylate (NaSal) in D_2O, where the micelles are approximately oriented along the flow direction. Although the following discussion centers around neutron scattering, the analyses discussed here can also be applied to other scattering methods, such as light and X-rays.

2. Method

2.1. Materials

CTAB, or hexadecyltrimethylammonium bromide, and NaSal were obtained from Sigma–Aldrich (St Louis, Missouri, USA) as powders. Deuterium oxide (D_2O, 99%) was purchased from Cambridge Isotope (Massachusetts, USA). CTAB and NaSal were stored at room temperature.

2.2. Sample preparation

A single solution of WLMs, containing 0.03 mol l^{-1} CTAB and 0.24 mol l^{-1} NaSal in D_2O (vol.% of 0.0125), was prepared for all measurements. A 20 ml sample solution was prepared at room temperature (~295 K) by combining CTAB and NaSal followed by addition of D_2O. The resulting solution was mixed by shaking vigorously for several minutes to dissolve the CTAB and NaSal. The sample was allowed to equilibrate for at least three days, during which any remaining visible powder dissolved. The now transparent sample was gently mixed to avoid bubble formation and allowed to rest for approximately four more days before measurement. The resulting solution shear thins with a relaxation time of λ_R = 2.27 s and a zero-shear viscosity of η_0 = 10.4 Pa s, where the rheological properties have been reported previously (Gilbert & Giacomin, 2019).

2.3. SANS techniques and modeling

SANS experiments were carried out using the D22 large dynamic range small-angle diffractometer at the Institut Laue–Langevin in Grenoble, France (Porcar & Gilbert, 2021). An Anton Paar MCR-501 rheometer was used as the sample environment (Krzywon, 2014). An 11.2 m detector distance was used for data collection over $0.006 \le q \le 0.06$ Å^{-1} with 6 Å neutrons, a 0.5 × 18 mm vertical-slit sample aperture and an acquisition time of 540 s. A detector distance of 17.6 m was used for data collection at $0.002 \le q \le 0.025$ Å^{-1} with 11.5 Å neutrons, a 10 × 14 mm sample aperture and a counting time of 480 s. The D22 small-angle diffractometer is equipped with a second detector fixed at 1.4 m that allows for simultaneous collection of high-q information ($0.02 \le q \le 0.35$ Å^{-1} when paired with the 17.6 m detector and $0.06 \le q \le 0.55$ Å^{-1} when paired with the 11.2 m detector). These detector distances allowed access to the full D22 instrument q range.

Data reduction was completed using *GRASP* (*Graphical Reduction and Analysis SANS Program*), a MATLAB script application (Dewhurst, 2003). *SasView* (Version 5.0.3; https://www.sasview.org/), an open-source scattering analysis program, was used for fitting the experimental data with a model for cylindrical particles (Doucet *et al.*, 2021). All anisotropy factor analysis and theoretical data generation

Version of Record at: https://doi.org/10.1107/S1600576723002182

were completed using MATLAB R2020A (implementation of this code in *SasView* is underway), where the cylinder model is documented by *SasView* (https://www.sasview.org/docs/user/models/core_shell_ellipsoid.html), and resolution functions and polydispersity parameters were implemented using equations from the *SANS Toolbox* (Hammouda, 2008). *GRASP* also has a `rheo_anisotropy` tool that comes equipped with some methods for calculating the anisotropy factor. Errors in parameter and intensity estimates are always presented as one standard deviation.

2.4. Rheometry and rheoSANS

To understand the relationship between particle orientation and rheological properties, techniques combining rheometry with SANS, called rheoSANS, are gaining popularity (Eberle & Porcar, 2012; Richards & Riley, 2019). Fig. 2 illustrates a typical rheoSANS setup with a Couette geometry, where the radial (beam passing through the middle of the cylinders) and tangential (beam passing through the gap between the cylinders) configurations offer two perspectives on particle orientation during flow. Each configuration produces a 2D scattering pattern from which orientation information can be extracted (Walker & Wagner, 1996; Corona *et al.*, 2021; Wang *et al.*, 2017). Fig. S1 in the supporting information shows the theoretically generated 2D scattering patterns and the measured 2D SANS patterns for the wormlike micelle solution used during analysis in this work.

RheoSANS is used in this work to align WLMs using a flow field. Three rheoSANS configurations are used to examine three micelle orientations $\theta_{\rm p}$, where $\theta_{\rm p}$ is the angle between the micelle and the neutron beam. Scattering patterns were produced at the radial ($\theta_{\rm p} = \pi/2$) and tangential ($\theta_{\rm p} = 0$) rheoSANS configurations, as well as at an intermediate configuration ($\theta_{\rm p} \simeq \pi/7$) between radial and tangential. The neutron beam is positioned at 24.5 mm from the center of the Couette geometry for the tangential configuration and 22 mm from the center for the intermediate configuration (Fig. 2). Scattering at different beam positions demonstrates the dependence of the anisotropy factor on WLM orientation relative to the neutron beam. The intermediate configuration at 22 mm produces the least intense anisotropic measurement achievable with the Couette rheometer setup and is the configuration nearest the tangential configuration, where tangential measurements should be isotropic.

An Anton Paar MCR-501 rheometer (Krzywon, 2014) fitted with a 50 mm diameter titanium cup and a 48 mm diameter titanium bob was used for all rheoSANS measurements. The WLM sample was carefully transferred to the cup, avoiding bubble formation. The solution was then brought to 298 K and presheared for one minute at a shear rate of 10 s^{-1} to remove any bubbles before measurement. A steady shear rate of 10 s^{-1} was used during rheoSANS measurement, as this is well within the shear thinning regime where WLMs are aligned (Gilbert & Giacomin, 2019). A homogenous flow field is assumed such that fluid elements at different vertical positions experience the same deformation.

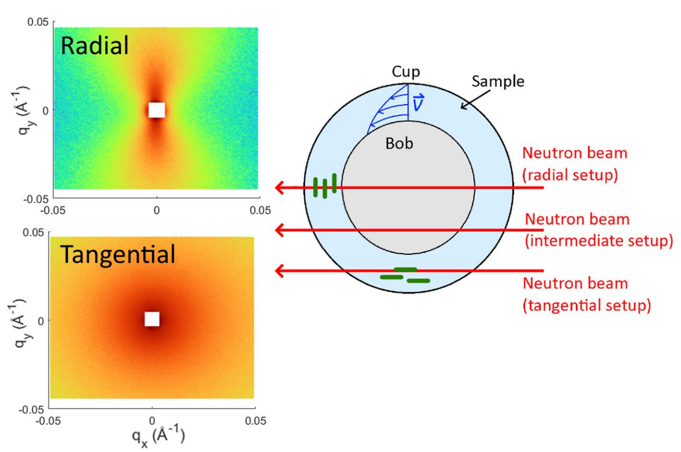

Figure 2
(Right) A top view of the steady-shear rheoSANS instrument setup for radial, intermediate and tangential configurations, with (left) corresponding example 2D scattering patterns for radial and tangential configurations, where the red arrows are the beam positions and the green particles represent approximate orientations in each configuration.

2.5. Theoretical scattering patterns

The absolute scattering intensity $I(q)$ for monodispersed spherical particles is

$$I(q) = \phi(\Delta\rho)^2 V_{\rm p} \tilde{P}(q)\, S(q) + B, \quad (1)$$

where ϕ is the volume fraction of the particles, $\Delta\rho$ is the difference in scattering length density (SLD) between the particle and the solvent, $V_{\rm p}$ is the particle volume, $\tilde{P}(q)$ is the normalized form factor, $S(q)$ is the inter-particle structure factor, q is the magnitude of the scattering vector, and B is the incoherent scattering background. Tables S1 and S2 in the supporting information summarize the dimensional and dimensionless variables, respectively. The scattering vector magnitude is defined as [see equation (3.7) of Sivia (2011)]

$$q \equiv \frac{4\pi \sin\theta_{\rm s}}{\lambda}, \quad (2)$$

where $\theta_{\rm s}$ is the half-angle between the scattered neutrons and the incident neutron beam, and λ is the neutron wavelength.

For a dilute suspension of non-isometric particles, $[S(q) \rightarrow 1]$, equation (1) becomes

$$I(q, \alpha) = \phi(\Delta\rho)^2 V_{\rm p} \tilde{P}(q, \alpha) + B, \quad (3)$$

where α is the angle between the primary particle axis and the scattering vector.

Equation (3) can be generalized for polydisperse suspensions, as well as for some non-spherical particles, using models that have been incorporated into modern data analysis programs such as *SasView* (Doucet *et al.*, 2021). Here, the cylinder model is used to approximate long thin oriented particles during theoretical analysis and data fitting. The form factor for a single cylinder of uniform composition is (https://www.sasview.org/docs/user/models/core_shell_ellipsoid.html)

$$P(q, \alpha) = \left|F(q, \alpha)\right|^2 = (\Delta\rho)^2 V_{\rm p}^2 \tilde{P}(q, \alpha). \quad (4)$$

$F(q,\alpha)$ is the form function,

$$F(q,\alpha) = 4(\Delta\rho)V_{\rm p}\,\frac{\sin(0.5qL\cos\alpha)}{qL\cos\alpha}\,\frac{{\rm J}_1(qR\sin\alpha)}{qR\sin\alpha}, \qquad (5)$$

where L is the cylinder length, R is the cylinder radius and J_1 is a first-order Bessel function of the first kind. By substituting equation (5) into equation (4), 2D scattering patterns for an oriented theoretical cylinder can be generated for anisotropy factor analysis [Fig. 1(*a*)]. Theoretical 2D scattering patterns were generated for a single cylindrical particle of radius 20 Å and length 1800 Å with and without 5% radial polydispersity. The choice of these parameters was based on fitting the experimental data.

The particle orientation relative to the incident neutron beam ($\mathbf{k}_{\rm i}$) is described by the polar angle $\theta_{\rm p}$ and the azimuthal angle $\phi_{\rm p}$, where the azimuthal angle is measured from the scattering axis normal to the incident beam–vorticity plane q_x. These orientation angles are illustrated in Fig. 3. The oriented particle scatters neutrons $\mathbf{k}_{\rm s}$ with angles $2\theta_{\rm s}$ and $\phi_{\rm s}$ also measured from $\mathbf{k}_{\rm i}$ and $\mathbf{x}$ (see Fig. 3); $\mathbf{k}_{\rm i}$ and $\mathbf{k}_{\rm s}$ are the incident and scattered neutron wavevectors, respectively. Together, these four angles ($\theta_{\rm p}$, $\phi_{\rm p}$, $\theta_{\rm s}$ and $\phi_{\rm s}$) define α:

$$\cos\alpha = -\sin\theta_{\rm p}\cos\theta_{\rm s}\cos\left(\phi_{\rm p}-\phi_{\rm s}\right) + \cos\theta_{\rm p}\sin\theta_{\rm s}. \qquad (6)$$

This geometric relationship is derived in Section S1 of the supporting information and agrees with equation (4.40) in the work of Fuller (1995). In the experimental rheoSANS example used in this work, $\theta_{\rm p} = 0$ corresponds to a rod parallel to the neutron beam, known as the rheoSANS tangential configuration. At $\theta_{\rm p} = \pi/2$, the rod is perpendicular to the neutron beam, corresponding to the radial rheoSANS configuration. The intermediate configuration at $\theta_{\rm p} = \pi/7$ is presented as an example of anisotropy factor dependence on cylinder tilt. Although a rheoSANS example is used here, the

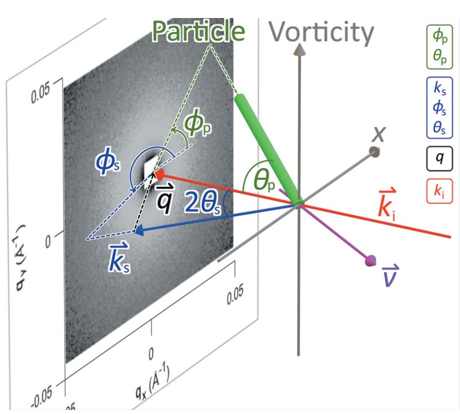

Figure 3
A schematic diagram showing the scattering vector $\mathbf{q}$ (black), the scattered wavevector $\mathbf{k}_{\rm s}$ (blue) and the particle orientation (green) relative to the incident beam $\mathbf{k}_{\rm i}$ (red), and the flow velocity vector $\mathbf{v}$ (violet), where $2\theta_{\rm s}$ and $\phi_{\rm s}$ are the radial and azimuthal angles, respectively, of the scattered wavevector and $\theta_{\rm p}$ and $\phi_{\rm p}$ are the radial and azimuthal angles, respectively, of the particle measured from the incident beam and the x coordinate or q_x axis. The x–vorticity plane of the rheometer is always perpendicular to the incident beam, where the q_y axis is parallel to the vorticity axis.

analysis applies to any rod-like particle or macromolecule oriented at different angles $\theta_{\rm p}$ relative to the source beam.

To clarify the effects of modern instrumentation constraints on anisotropy factor calculations, theoretical scattering patterns are generated with infinite resolution [exact calculation of equation (4)], with finite detector grid spacing [Fig. 1(*a*)], with realistic smearing [Fig. 1(*b*)] or with radial polydispersity [Fig. 1(*c*)]. Smearing is used to approximate the real instrument resolution according to the *SANS Toolbox* by convoluting the 2D pattern with the Gaussian resolution function [equation (19.1) in the work of Hammouda (2008)],

$$g(q) = \frac{1}{\sigma_q(2\pi)^{1/2}}\exp\left(-\frac{q^2}{2\sigma_q^2}\right), \qquad (7)$$

where σ_q^2 is the variance of the q resolution typically corresponding to a 15% distribution in q. Grid spacing effects are probed by adjusting the point spacing over a specified q range. When included in the model, polydispersity is set at 5% with a Gaussian distribution [see equation (5) in ch. 29 of Hammouda (2008)].

2.6. Anisotropy factor equations

Three commonly used methods for estimating anisotropy factor are featured as examples in this work, and the calculation details are summarized here. The cosine expansion method weights the annular average of the scattering data with $\cos 2(\phi_{\rm s}-\phi_{\rm s,0})$ (Walker, 1995),

$$A_{\rm f,cos}(q) = \frac{\int_0^{2\pi} I(q,\phi_{\rm s})\cos 2\left(\phi_{\rm s}-\phi_{\rm s,0}\right){\rm d}\phi_{\rm s}}{\int_0^{2\pi} I(q,\phi_{\rm s})\,{\rm d}\phi_{\rm s}}, \qquad (8)$$

where $\phi_{\rm s,0}$ is the reference angle corresponding to the angle of the intensity peaks and $\phi_{\rm s} = 0$ corresponds to the negative q_x axis (*e.g.* negative flow axis). Equation (8) has a lower limit of -1, indicating scattering only perpendicular to $\phi_{\rm s,0}$ (along the flow direction), and a positive limit of 1 for scattering only along $\phi_{\rm s,0}$. The anisotropy factor is zero for isotropic scattering. For our analysis, $\phi_{\rm s,0}$ is set to $\pi/2$ and is perpendicular to the flow direction.

The Legendre expansion method uses the second-order Legendre polynomial to weight the annular averaged scattering data, so that (Hongladarom *et al.*, 1996; Rosén *et al.*, 2018; Lemaire *et al.*, 2004)

$$A_{\rm f,L}(q) = \frac{\int_0^{\pi} I(q,\phi_{\rm s})\left[\frac{3}{2}\cos^2\left(\phi_{\rm s}-\phi_{\rm s,0}\right)-\frac{1}{2}\right]\sin\left(\phi_{\rm s}-\phi_{\rm s,0}\right){\rm d}\phi_{\rm s}}{\int_0^{\pi} I(q,\phi_{\rm s})\sin\left(\phi_{\rm s}-\phi_{\rm s,0}\right){\rm d}\phi_{\rm s}}. \qquad (9)$$

Here $\phi_{\rm s,0}$ is the reference angle corresponding to the angle of the intensity peaks and $\phi_{\rm s} = 0$ corresponds to the negative q_x axis (*e.g.* negative flow axis). Equation (9) can be applied to discs [see Fig. 1 of Liebi *et al.* (2013)] and long cylinders (Lovell & Mitchell, 1981). Equation (9) has a lower theoretical limit of $-\frac{1}{2}$ when scattering only occurs along the flow direction (or magnetic field) and an upper theoretical limit of 1 for scattering only perpendicular to the flow (along $\phi_{\rm s,0}$).

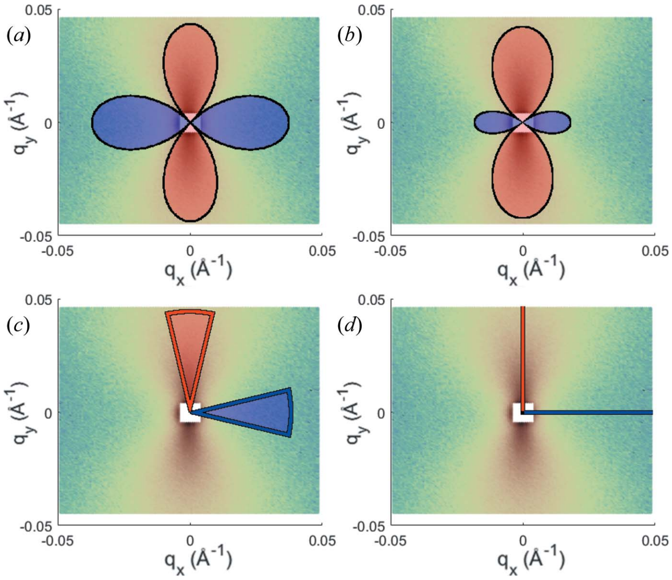

Figure 4
Weighting functions for each of the four A_f calculation methods: (*a*) cosine expansion, (*b*) Legendre expansion, (*c*) axial sector integration and (*d*) axial linear integration. The distance from the center of the scattering pattern represents the relative weighting magnitude. Scattering intensity within the red sections increases the anisotropy factor, while intensity within the blue sections reduces the anisotropy factor.

Both expansion-based methods produce an anisotropy factor that is dependent on q. The weighting functions for these methods are visualized in Figs. 4(*a*) and 4(*b*).

The axial integration methods only consider intensity data near the axes perpendicular, $I_\perp$, and parallel, $I_\parallel$, to the director (flow direction) (Pujari *et al.*, 2011; Iwase *et al.*, 2019),

$$A_{\rm f,int} = \frac{\int_{q_{\min}}^{q_{\max}} I_\perp(q)\,{\rm d}q - \int_{q_{\min}}^{q_{\max}} I_\parallel(q)\,{\rm d}q}{\int_{q_{\min}}^{q_{\max}} I_\perp(q)\,{\rm d}q}, \quad (10)$$

where $q_{\max}$ and $q_{\min}$ are, respectively, the maximum and minimum of the q range of interest, which can be adjusted to probe different length scales. Figs. 4(*c*) and 4(*d*) visualize the sector and linear integrations of equation (10). The form of equation (10) is chosen for the present analysis, but axial integration methods may take different mathematical forms (Pujari *et al.*, 2011). In a perfectly aligned system, the perpendicular integration is along the intensity peak while the parallel integration is along the trough in the intensity, corresponding to cylinder orientation. $A_{\rm f,int} = 1$ corresponds to perfect alignment along the director, while $A_{\rm f,int} = -\infty$ corresponds to perfect alignment perpendicular to the director. Although an anisotropy factor of 0 corresponds to isotropic scattering for any calculation method, the positive and negative limits can be different. Practitioners must take care to evaluate the amount of anisotropy reported from their chosen calculation method using the limits specified for that method.

Equation (10) was evaluated using trapezoidal numerical integration over the q range of interest. Intensity data were either extracted from the row/column of data closest to the axes or averaged using angular sectors near each axis, where the angular sector width is $\Delta\phi_{\rm sect} = 2|\phi_{\rm sect}|$. An angular sector is centered at a specific azimuthal scattering angle $\phi_{\rm s}$ and its boundaries are determined by $\pm\phi_{\rm sect}$.When $\phi_{\rm sect} = 0°$, the integration becomes a simple line integration along a scattering angle. In the case of axial integration, $\phi_{\rm s} = 0$ or $\phi_{\rm s} = \pi/2$. As the integration range influences the estimate of the anisotropy factor, the necessary q range for reaching a characteristic anisotropy factor was evaluated by breaking the integration range into sections. This analysis also discusses the effects of including more data along each axis by using angular sectors. Linear integration is approximated using data that fall within a 0.002 Å^{-1} wide rectangle along each axis.

3. Results

This section is organized by anisotropy factor calculation method: expansion methods and axial integration methods. The limitations on q range, instrument resolution and detector grid spacing are examined for each method, as these three parameters influence the estimated value of the anisotropy factor. The q range determines which data will be included in the analysis, while the instrument resolution and detector grid spacing determine how the data must be binned. Anisotropy factor calculation methods are compared by applying them to theoretically generated data for a perfectly aligned dilute suspension of cylinders with and without resolution smearing and radial polydispersity. Each method is also used to analyze experimental scattering data for a WLM solution of CTAB and NaSal undergoing steady shear flow.

3.1. Theoretical and experimental SANS patterns

Three sets of theoretical data for an oriented cylinder were generated using equations (4) and (5): without instrument resolution effects or polydispersity [Fig. 1(*a*)], with relative instrument q resolution of 15% [Fig. 1(*b*)], and with both instrument resolution effects and 5% radial polydispersity [Fig. 1(*c*)]. Scattering is calculated for a cylinder that is perfectly oriented along the horizontal flow direction. A horizontal rod orientation ($\theta_{\rm p} = \pi/2$, $\phi_{\rm p} = 0$) leads to an intense vertical scattering streak in each of the scattering patterns. Fig. 1(*a*) represents a 2D scattering pattern with nearly perfect resolution, where the resolution is only limited by the finite detector grid spacing. This grid spacing represents the finite 'pixelation' of the detector. Without smearing by the resolution or the particle size polydispersity, the scattering pattern has significant Fourier ringing, where the intensity goes through periodic peaks and valleys with increasing q. This ringing is related to the cylinder morphology, where ringing along q_x results from the monodisperse length.

A Gaussian resolution function is added to Fig. 1(*a*) using a scattering vector distribution of 15% rather than a monodisperse q. This smearing smooths some of the ringing in the intensity, resulting in Fig. 1(*b*) where the intensity valleys and peaks are less dramatic. Inclusion of the resolution function reflects scattering vector distributions in real instrumentation.

Version of Record at: https://doi.org/10.1107/S1600576723002182

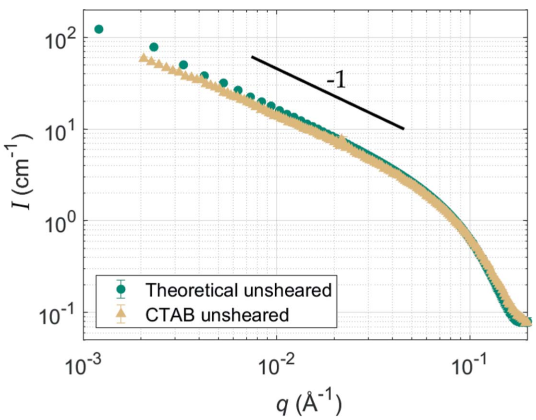

Figure 5
One-dimensional scattering intensity curves for a theoretical suspension of monodisperse cylindrical particles having a length of 1800 Å and an average radius of 20 Å with 5% radial polydispersity and from experimental SANS results for a randomly oriented CTAB/NaSal WLM solution, where all curves demonstrate the characteristic slope of −1 for cylinders. Error bars represent one standard deviation.

A small amount (5%) of radial polydispersity is added to the cylinders to simulate a real sample, resulting in further smoothing of the 2D scattering pattern [Fig. 1(*c*)]. Each of these scattering patterns is used to examine the effects of instrument non-ideality on anisotropy factor analysis in the following sections. Fig. 5 shows the 1D scattering curve for a randomly oriented polydisperse cylindrical form factor with smearing, where there is a slope of −1 for cylindrical morphologies at $0.002 \le q \le 0.04$ Å^{-1}. This is compared with the 1D scattering curve for a quiescent WLM solution of 0.03 mol l^{-1} CTAB and 0.24 mol l^{-1} NaSal in D_2O. The theoretical data were generated to be an approximate match for the size of the CTAB/NaSal WLMs.

3.2. Estimating anisotropy with expansion methods

Before equations (8) and (9) can be applied to scattering data, the q range of interest must be selected, and an annular average over the selected q range is required to obtain the scattering intensity as a function of the azimuthal scattering angle $I(\phi_s)$. Considerations for choosing an appropriate annular region include the selection of inner and outer annular radii (q range), the organization of data into equally sized bins (resolution along ϕ_s), and accounting for the detector resolution or grid spacing (q_x and q_y). Each of these topics is examined in the following subsections. An example annular average is drawn in Fig. 1(*b*), where the intensity data in the shaded annular region are averaged at each value of ϕ_s. Fig. 1(*d*) is an example of an $I(\phi_s)$ versus ϕ_s plot resulting from an annular average of $0.015 \le q \le 0.02$ Å^{-1} for the theoretical data in Figs. 1(*a*)–1(*c*). In each case, sharp intensity peaks occur at $\phi_s = \pi/2$ and $3\pi/2$, indicating particle alignment along the horizontal flow direction at $\phi_s = 0$. The peaks are narrowest for the unsmeared data and broaden with the addition of resolution effects and polydispersity. This peak broadening caused by resolution effects and polydispersity corresponds to a lower anisotropy factor, even though the physical alignment of particles in the system has not changed. Thus, resolution effects and particle size polydispersity do not affect particle alignment, but they do influence the anisotropy factor.

3.2.1. Anisotropy factor dependence on scattering vector. A_f for a rod perpendicular to the neutron beam ($\theta_p = \pi/2$) is plotted versus the dimensionless scattering vector qL in Figs. 6(*a*)–6(*c*) for the cosine and Legendre expansions using equations (4), (8) and (9). A_f is calculated exactly for each q value with perfect resolution. Thus, the annulus used to produce $I(\phi_s)$ is very thin, approaching a circle. The cosine and Legendre calculation methods agree on the dependence of A_f on qL for all rod lengths and radii when considering only a single rod. There are three characteristic regions of A_f dependence on qL: $qL < 2\pi$, $2\pi \le qL \le j_{1,1}L/R$ and $j_{1,1}L/R < qL$, where $j_{1,1}$ is the first positive zero of the first-order Bessel function of the first kind (∼3.83) and R is the radius of the cylinder. When $qL < 2\pi$, A_f approaches zero. This is a mathematical limit at low q for equations (8) and (9), where $qL < 2\pi$ probes length scales greater than the length of the cylinder. Thus, the scattering pattern is no longer sensitive to particle orientation in this range of q, and anisotropy factors calculated below this limit are not representative of the cylinder's

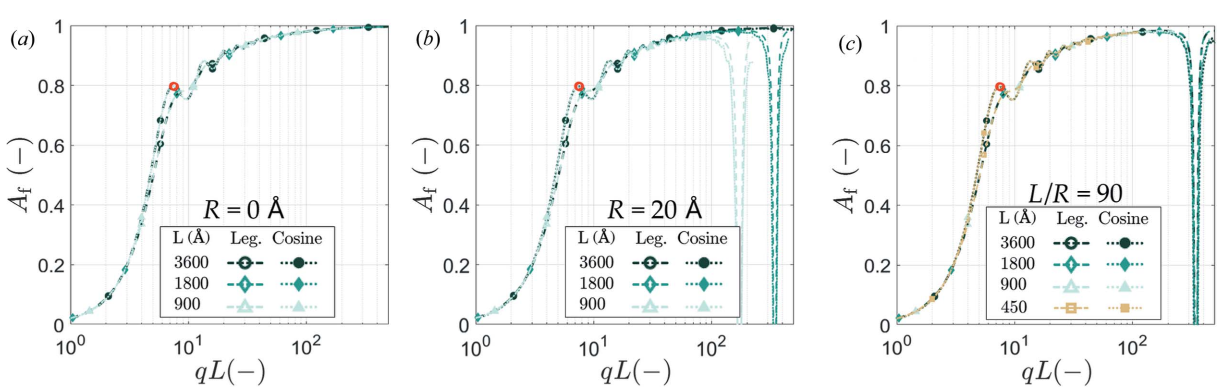

Figure 6
Cosine [equation (8)] and Legendre expansion [equation (9)] anisotropy factor calculations versus the dimensionless scattering vector qL for the exact form factor at $\theta_p = \pi/2$ of a cylinder [equation (4)] having $L = 1800$ Å and radius (*a*) $R \to 0$ Å or (*b*) $R = 20$ Å, and (*c*) for rods having different lengths with constant aspect ratio $L/R = 90$. The red circles at low qL correspond to $qL = 2\pi$ and the asymptotes at high qL occur at $qL/R = j_{1,1}L/R$.

alignment. The open red circles in Figs. 6(*a*)–6(*c*) correspond to the transition at $qL = 2\pi$ between the asymptotic drop of A_f to 0 and the plateau of maximal A_f.

Fig. 6(*b*) reveals a limit at high q, where A_f approaches an asymptote at $qR = j_{1,1}$, above which q probes lengths smaller than the cylinder radius. Thus, the cylinder radius defines a typical upper bound for annular averaging. Fig. 6(*c*) confirms that the q dependence of the anisotropy factor collapses onto a single curve in dimensionless qL space for cylinders having the same aspect ratio. Each curve has limiting behavior at $qL = 2\pi$ and at $qL = j_{1,1}L/R$. Thus, when analyzing the alignment of a single rod, the q range selected for the annular average should typically fall between $qL = 2\pi$ and $qR = j_{1,1}$. Other q ranges may be selected for analysis, but care must be taken to determine which morphological features (*i.e.* groups of rods, gaps between rods) are being probed.

The anisotropy factor reported in Fig. 6(*a*) is for a perfectly aligned cylinder with infinitesimal radius ($R \to 0$ Å) using a detector with perfect resolution. It is expected that perfect alignment would result in an anisotropy factor of 1. For an infinitely thin rod, the anisotropy factor only approaches 1 above $qL \simeq 200$, which is larger than $qL = 2\pi$. Thus, to achieve an anisotropy factor of 1, q values above ∼0.2, 0.1 and 0.05 Å^{-1} would need to be selected for rod lengths of 90, 180 and 360 nm, respectively. Any q value below this would result in a reduced anisotropy factor using either the cosine or the Legendre method.

Fig. 6(*b*) reports the anisotropy factor for perfectly aligned cylinders of finite radius (R = 2 nm) and lengths matching those of Fig. 6(*a*). Under these ideal conditions for a finite rod, A_f does not reach 1 over the typical range, $2\pi \le qL \le j_{1,1}L/R$, for any cylinder length. Additionally, A_f varies with qL within this range and has a maximum at $qL = 1.84L/R \simeq j_{1,1}L/D$, where D is the rod diameter. When available, intensity data at $qL \simeq j_{1,1}L/D$ should be included in the annular average to produce a representative maximum A_f. As the aspect ratio (L/D) decreases, the peak in A_f is reduced and shifted to lower qL. This reveals the dependence of A_f on particle morphology, where aspect ratios approaching unity will result in $A_f \to 0$.

Two guidelines for selecting a q range over which an annular average should be calculated for rod-like particles arise from the results in Figs. 6(*a*)–6(*c*):

(i) One should maximize the available range for the anisotropy factor and $qL \simeq j_{1,1}L/D$ should be included within the selected q range.

(ii) Typically, the selected q range should fall within $2\pi \le qL \le j_{1,1}L/R$.

These are only guidelines, as anisotropy factor analysis can be conducted over any q range. For example, these criteria would suggest including all the 2D scattering data of Fig. 1(*a*), except at q < 0.003 Å^{-1}, within the annular average to get a single representative anisotropy factor. It may be of interest to analyze instead specific features within Fig. 1(*a*) by selecting a more restricted q range, but this may not yield a representative anisotropy factor for the scattering pattern.

If a rod is tilted along the beam axis ($0 < \theta_p < \pi/2$) while being perfectly aligned, the projection of the rod must be used as the characteristic length L_c instead of the actual length L. This projected length cross section is

$$L_c = L \sin\theta_p + 2R\cos\theta_p. \tag{11}$$

Annular averaging of the scattering from a tilted rod cross section follows the same typical guidelines for q-range selection of $2\pi \le qL_c \le j_{1,1}L_c/R$. Because L_c is always smaller than L ($L_c/R < L/R$), rod tilt will reduce the typical range available for producing an annular average by lowering the maximum q limit.

Adding finite detector grid spacing, smearing or rod polydispersity also reduces the q range available for annular averaging and suppresses the value of the resulting anisotropy factor. The effects of non-ideality are discussed in more detail below in Section 3.2.3.

3.2.2. Binning scattering data for annular averaging. Once the q range available for annular averaging has been determined using the conditions developed in the previous section, the practitioner must decide how much data will be included in the annular average to produce a plot of $I(q)$ versus azimuthal scattering angle ϕ_s [Fig. 1(*d*)]. This subsection provides guidelines on annulus size selection for annular averaging of 2D data while accounting for finite detector grid spacing and data binning. This is particularly important when analyzing data at low q, where there are few detector pixels.

The annular area A_A is defined as

$$A_A = 2\pi\overline{q}\Delta q, \tag{12}$$

where $\overline{q}$ is the average q within the annulus, $(q_{max} + q_{min})/2$, and Δq is the q range included in the annular average, $q_{max} - q_{min}$. Thus, a larger Δq or $\overline{q}$ corresponds to a larger annular area. Annular area selection is especially important for producing q-dependent anisotropy factor analyses, as practitioners must decide how many data points need to be included in an annulus to produce a representative anisotropy factor estimate for a particular value of q. Special care must be taken when selecting an annulus size for regions containing few data points, which occurs frequently in q ranges near the beam stop or beam center.

Bin count refers to the number of equally sized bins that segment the annular area along its circumference, where each bin corresponds to an average azimuthal scattering angle ϕ_s. Fig. 1(*b*) illustrates an example set of 16 bins within an annulus. A higher bin count decreases the ϕ_s spacing and reduces the number of data points included in each bin. For this analysis, each bin must contain at least one data point, representing a necessary condition on annular area and maximum bin count. Thus, as the bin count increases so must the annular area. At low bin counts, the bins must be centered on and perpendicular to the scattering intensity streak [vertical axis of Figs. 1(*a*)–1(*c*)]. This can only be achieved for bin counts that are multiples of four, which is a second necessary condition at low bin count. Practitioners should be particularly mindful of the bin count when analyzing data at small q or in q ranges near the beam stop, as the finite detector pixel size may limit the availability of data. This also means

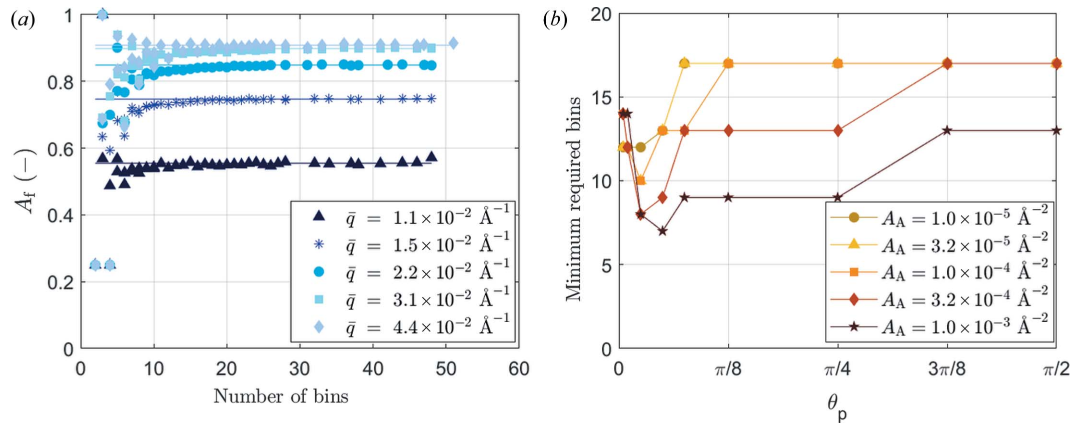

Figure 7
(a) Anisotropy factor dependence on bin count for annular averaging using theoretical data with smearing at $\theta_p = \pi/2$ with an annular area of $A_A = 10^{-4}$ Å^{-2}, where the anisotropy factor is constant above a sufficient minimum bin count of 20 at all average scattering vector magnitudes $\bar{q}$. (b) The dependence of the minimum bin count on the particle orientation angle θ_p, where $\theta_p = \pi/2$ corresponds to the radial configuration and $\theta_p = 0$ the tangential.

that larger annular areas may be needed to include sufficient data.

To determine the minimum number of bins, the anisotropy factor was calculated at several $\bar{q}$ for theoretically generated 2D scattering patterns [Figs. 1(a)–1(c)]. The annular area was fixed at 10^{-4} Å^{-2} (or $\Delta q = 10^{-4}/2\pi\bar{q}$ Å^{-1}), allowing for at least one data point in each bin at all $\bar{q}$. Fig. 7(a) shows how the cosine expansion estimate of the anisotropy factor depends on the bin count at different $\bar{q}$. The anisotropy factor approaches a limiting, or representative, value at sufficiently large bin count. It was found that at least 20 bins are required to produce a representative anisotropy factor estimate at $\bar{q}$ = 0.044 Å^{-1}. As $\bar{q}$ decreases, the minimum number of bins becomes smaller, where only approximately eight bins are needed at $\bar{q}$ = 0.011 Å^{-1}. However, it is recommended that at least 20 bins are used during annular averaging to guarantee a representative anisotropy factor estimate at any $\bar{q}$.

When the rod is not perpendicular to the neutron beam ($\theta_p \neq \pi/2$), the required number of bins can be less than 20. Fig. 7(b) shows the dependence of the minimum bin count on θ_p and annular area. With the exception of the smallest annular area, at least 20 bins are needed to produce a representative anisotropy factor estimate at $\theta_p \geq \pi/4$. At smaller angles, the bin count may decrease to ~12 or 16, especially for smaller annular areas. However, in all cases at least 20 bins should be used, if possible, to guarantee a representative anisotropy factor estimate. If achieving 20 bins is not possible, Fig. 7(b) can be used to select a reliable lower bin count.

3.2.3. Effects of detector grid spacing, smearing and polydispersity. The inclusion of a finite grid spacing (d = 0.001 Å^{-1}), 15% smearing from the scattering vector spread ($\Delta q/q$ = 0.15) and 5% radial polydispersity in the calculation of A_f results in the green $A_f(\bar{q})$ curves shown in Fig. 8 for (a) the cosine and (b) the Legendre expansions using the theoretical scattering data of Fig. 1(c). The bin counts and annular areas used in the A_f calculations of Fig. 8 are summarized in Fig. S2 of the supporting information. Twenty bins are used at all $\bar{q}$, except at low $\bar{q}$ where the sparsity of data reduces the number of bins. The reduced bin count probably results in the non-zero Legendre expansion anisotropy factor at low $\bar{q}$ in Fig. 8(b). However, the cosine expansion in Fig. 8(a) seems to handle fewer bins more reliably as there is no deviation from zero at low $\bar{q}$. Further discussion of the relationship between bin count, annular area and anisotropy factor can be found in Section S2 of the supporting information.

The red dashed curves in Fig. 8 correspond to the exact anisotropy factor calculations for a perfectly aligned cylinder at $\theta_p = \pi/2$ with 5% polydispersity using equations (8) and (9). The maximum plateaux of the red curves fall within the recommended limits of $2\pi \leq qL \leq j_{1,1}L/R$ ($0.0035 \leq q \leq 0.19$ Å^{-1}) identified in Section 3.2.1. The red dashed curves in Fig. 8 only reach a maximum of $A_f \simeq 0.9$, whereas the perfectly resolved and monodisperse curves in Fig. 6(b) approach $A_f = 1$ within the recommended q range. Thus, the inclusion of 5% radial polydispersity reduces the calculated anisotropy factor,

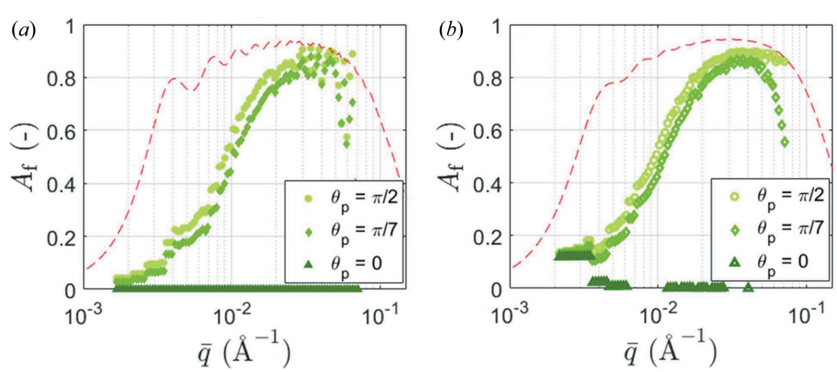

Figure 8
(a) Cosine and (b) Legendre expansion calculations of anisotropy factor for a 15% smeared 2D theoretical scattering pattern with cylindrical particles having L = 1800 Å, R = 20 Å and 5% radial polydispersity, where the bin counts used for the calculations are reported in Fig. S2. The red dashed lines indicate the anisotropy factor calculated directly from equations (4), (8) and (9) at $\theta_p = \pi/2$ with 5% radial polydispersity.

even though the rods in both Fig. 6(*b*) and Fig. 8 are perfectly aligned. In this way, the inclusion of polydispersity decreases the anisotropy factor for all q despite the rod alignment remaining unchanged.

The limitations of modern SANS equipment must be considered during analysis as they can influence the calculated anisotropy factor, even for perfectly aligned systems. Comparing the red dashed curves and the green curves in Fig. 8 reveals that the inclusion of a finite detector resolution or grid spacing of $d = 0.001$ Å^{-1} and scattering vector smearing makes the A_f peak narrower and smaller. Thus, detector resolution and smearing effects constrain the q range available for anisotropy factor analysis, where the maximum A_f plateau is restricted to $0.02 \lesssim \overline{q} \lesssim 0.05$ Å^{-1}. Specifically, smearing and detector resolution effects reduce the maximum anisotropy factor peak by 2.93% for the cosine expansion method and shift the peak by 0.0091 Å^{-1}. For the Legendre expansion method, the A_f peak is reduced by 5.00% and shifted by 0.0085 Å^{-1}. Both methods produce A_f values that are within a typical 5% tolerance of the expected value (red curve).

The peaks of the green curves in Fig. 8 are shifted to lower $\overline{q}$ compared with the perfectly resolved curves of Fig. 6, where the maximum A_f occurs at $qL = 1.84L/R \simeq j_{1,1}L/D$ or $\overline{q} = 0.092$ Å^{-1}. The peak of the red curve in Fig. 8 is also shifted to lower $\overline{q}$, suggesting that radial polydispersity shifts the peak position and reduces the peak maximum. Resolution effects further reduce the calculated anisotropy factor but shift the peak position closer to that of perfectly resolved data (higher $\overline{q}$). Practitioners must account for this resolution effect, as anisotropy factors less than 1 can correspond to perfect particle alignment when their data are not perfectly resolved.

It is often necessary to consider rod tilt relative to the neutron beam in anisotropy factor analysis. As the rod becomes less perpendicular to the neutron beam, the anisotropy factor decreases, regardless of rod alignment relative to the director (*i.e.* flow direction). When the beam and rod are parallel ($\theta_\mathrm{p} = 0$), the anisotropy factor approaches 0. In Figs. 8(*a*) and 8(*b*), the anisotropy factor decreases with changing rod orientation from a maximum of $A_\mathrm{f} \simeq 0.85$ at $\theta_\mathrm{p} = \pi/2$ to $A_\mathrm{f} \simeq 0.82$ at $\theta_\mathrm{p} = \pi/7$, where $\theta_\mathrm{p} = \pi/7$ corresponds to a rod that is oriented at an angle of $\pi/7$ relative to the neutron beam. Practitioners must be aware that molecular and particle tilt relative to the beam can influence the anisotropy factor analysis. The green curves in Fig. 8 also reveal that detector resolution, smearing effects and polydispersity reduce the value of the anisotropy factor for all nonzero θ_p.

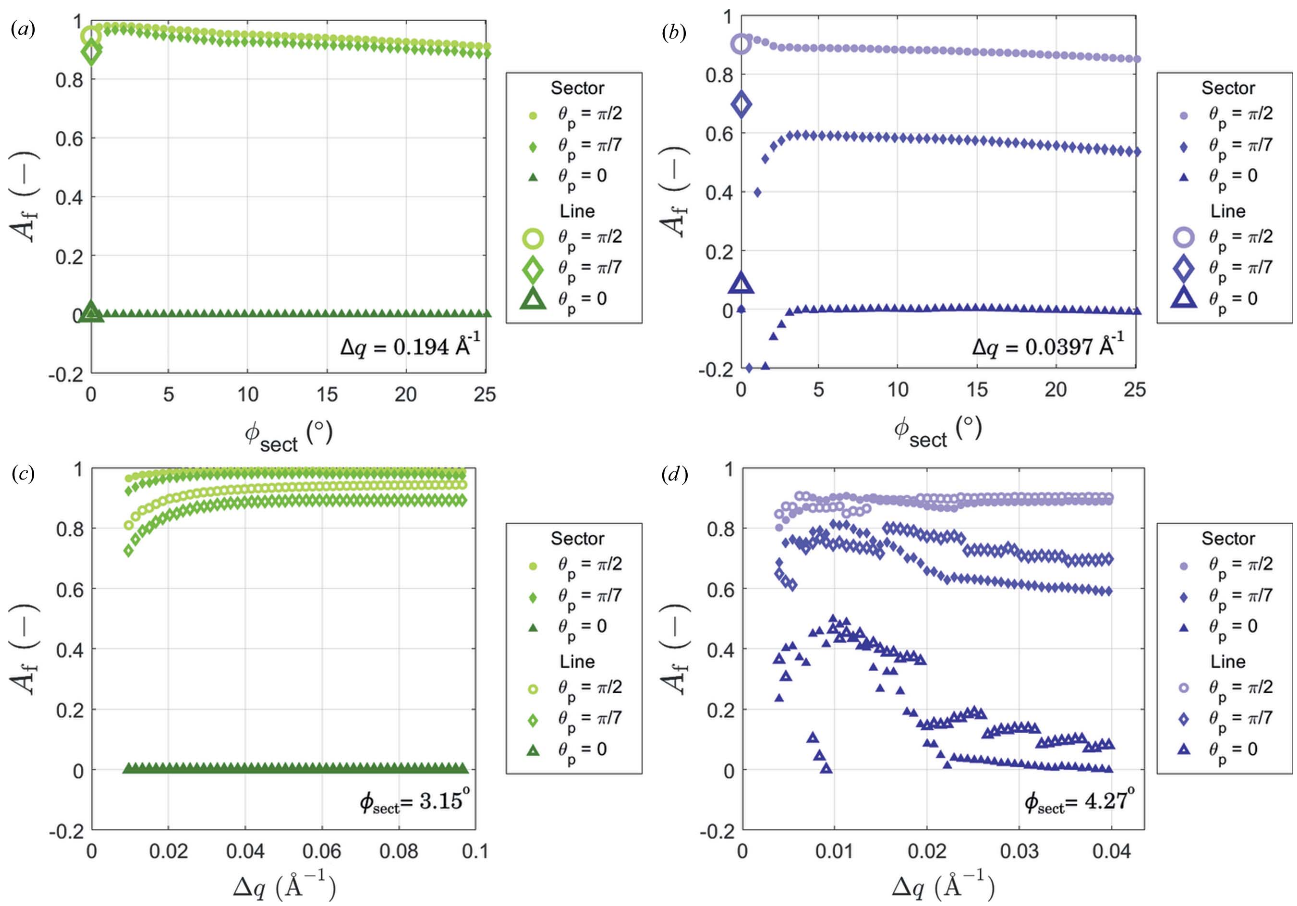

Figure 9
Anisotropy factors estimated from the integrated axis method at $\theta_\mathrm{p} = \pi/2, \pi/7, 0$ versus sector angle ϕ_sect and annular width Δq for (*a*), (*c*) theoretical cylindrical particles of $L = 1800$ Å and $R = 20$ Å, and (*b*), (*d*) a CTAB/NaSal WLM solution. The anisotropy factors for theoretical data are nearly invariant with (*a*) ϕ_sect and (*c*) Δq, while the anisotropy factors for experimental data change with (*b*) ϕ_sect and (*d*) Δq. In panels (*c*) and (*d*), a sector angle of ϕ_sect = FWHM/10 is chosen to illustrate the influence of Δq on anisotropy factor estimates.

3.3. Axial integration methods

Axial methods estimate the anisotropy factor by integrating the scattering intensity over a range of q along the axes perpendicular and parallel to the intensity peak. Intensity data off the axes can be included by performing a sector average within a specified angle relative to each axis (*e.g.* $\phi_{\rm sect} = \pm 7^\circ$ or $\Delta\phi_{\rm sect} = 14^\circ$) (Iwase *et al.*, 2019; Andriano *et al.*, 2020; Gazeau *et al.*, 2002) or by using a rectangular area along each axis. The effects of selected q range (Δq) and sector half-width ($\phi_{\rm sect}$) on the estimate of the anisotropy factor are examined here for theoretical and experimental data.

The anisotropy factor calculated directly using the form factor in equations (4) and (5) for a cylinder of $L = 180$ nm and $R = 2$ nm is considered first [Fig. S3(*a*)]. For this ideal scattering pattern, $A_{\rm f}$ from integration along the q_x and q_y axes is 0.998 [Fig. S3(*b*)], where the sector width is zero ($\phi_{\rm sect} = 0^\circ$) and the included q range is $\Delta q = 0.188$ Å^{-1}. There is virtually no change (<3%) in the estimate of $A_{\rm f}$ with increasing Δq from 0.001 to 0.188 Å^{-1}, where the latter corresponds to the maximum range available ($2\pi \le qL \le j_{1,1}L/R$ or $0.0035 \le q \le 0.192$ Å^{-1}). This invariance of $A_{\rm f}$ with Δq is illustrated in Fig. S3(*b*). As $A_{\rm f}$ does not change significantly with Δq, it is recommended that the maximum available q range be included in the integration up to the typical limits of $2\pi \le qL \le j_{1,1}L/R$.

Figs. 9(*a*) and 9(*c*) illustrate the effect of $\phi_{\rm sect}$ and Δq on estimates of $A_{\rm f}$ from theoretical data with finite detector grid spacing and smearing effects. From line integration ($\phi_{\rm sect} = 0^\circ$) $A_{\rm f} = 0.9$, which is smaller than the value of $A_{\rm f} = 0.998$ from line integration of the infinitely resolved form factor. This agrees with observations for the expansion methods, where the inclusion of smearing and finite detector grids reduced the anisotropy factor. When the sector angle is increased from 0 to 1°, there is an increase in the anisotropy factor for $\theta_{\rm p} > 0$ [Fig. 9(*a*)]. $A_{\rm f}$ is insensitive to sector size at sector angles within $3 \le \phi_{\rm sect} \le 13^\circ$. $\phi_{\rm sect} = 31.5^\circ$ corresponds to the FWHM of the I versus $\phi_{\rm s}$ curve, while $\phi_{\rm sect} = 3.15^\circ$ is one-tenth of the FWHM. Thus, it is recommended to select sector angles within FWHM/$10 \le \phi_{\rm sect} \le$ FWHM.

Fig. 9(*c*) shows that $A_{\rm f}$ for theoretical data is invariant with Δq for both linear and sector ($\phi_{\rm sect} = \pm 3.15^\circ$) integrations. For all Δq and $\phi_{\rm sect}$, the $A_{\rm f}$ of theoretical data does not deviate from 0 at $\theta_{\rm p} = 0$. Thus, integrated axis methods report anisotropy factor values that are less dependent on q than their expansion method counterparts when applied to theoretical data.

3.4. Alignment of wormlike micelles

The anisotropy factor was estimated for a CTAB/NaSal WLM solution subjected to a shear rate of 10 s^{-1} over $0.011 \le \overline{q} \le 0.043$ Å^{-1} using the cosine expansion, the Legendre expansion and the axial integration method (Fig. 10). Fig. S4 summarizes the annular areas used in the expansion-method calculations. Axial integrations were performed over the full available q range, because the measurement range of $0.005 \le q \le 0.057$ Å^{-1} falls entirely within $2\pi \le qL \le j_{1,1}L/R$ (or $0.0035 \lesssim q \lesssim 0.192$ Å^{-1}). This results in a single estimate of $A_{\rm f}$ for all measured q when using integration methods. Fig. 9(*d*) shows that $A_{\rm f}$ calculated from the integrated axis methods for experimental data can be strongly influenced by Δq. For $\theta_{\rm p} = \pi/2$, $A_{\rm f}$ converges to a single value of ∼0.9 at $\Delta q > 0.02$ Å^{-1}. For $\theta_{\rm p} = 0$, $A_{\rm f}$ ranges from ∼0.45 to 0 over the examined Δq range, where $A_{\rm f}$ approaches the expected value of 0 at $\Delta q > 0.02$ Å^{-1}. This suggests that it is best to maximize Δq when estimating $A_{\rm f}$ using axial integration methods.

In Fig. 10, radial configuration ($\theta_{\rm p} = \pi/2$) scattering for the WLM solution results in a nearly constant anisotropy factor of ∼0.55 over the entire q range for both expansion methods. For the same WLM solution, axial methods produce anisotropy factors of ∼0.90 for linear integration and ∼0.88 for sector integration, where $\phi_{\rm sect} = 4.25^\circ$. Fig. 9(*b*) shows that the anisotropy factor is weakly dependent on sector angle within $3 \le \phi_{\rm sect} \le 13^\circ$. Linear and sector axial methods produce anisotropy factors with a 3% difference, but axial methods estimate an $A_{\rm f}$ nearly double that of expansion methods. This is probably caused by the inclusion of more intensity data in expansion method calculations and, specifically, data at angles that lie on the axes.

$A_{\rm f}$ is lower for smaller orientation angles ($\theta_{\rm p}$), where $A_{\rm f} \to 0$ as $\theta_{\rm p} \to 0$, because the apparent length cross section becomes smaller with decreasing $\theta_{\rm p}$ [see equation (11)]. Estimates of $A_{\rm f}$ are nearly independent of $\overline{q}$ at $\theta_{\rm p} = \pi/2$ and $\theta_{\rm p} = 0$ when using expansion methods, but when the WLMs are tilted ($\theta_{\rm p} = \pi/7$) $A_{\rm f}$ decreases with $\overline{q}$. The $\overline{q}$ dependence of $A_{\rm f}$ at $\theta_{\rm p} = \pi/7$ may arise from the tilted perspective on the length cross section or the orientation distribution. The expansion methods agree with each other for all $\theta_{\rm p}$, but they estimate an $A_{\rm f}$ that is smaller than estimates from axial methods at $\theta_{\rm p} > 0$. As was suggested in the previous paragraph, this is probably caused by the inclusion of more data in the expansion methods,

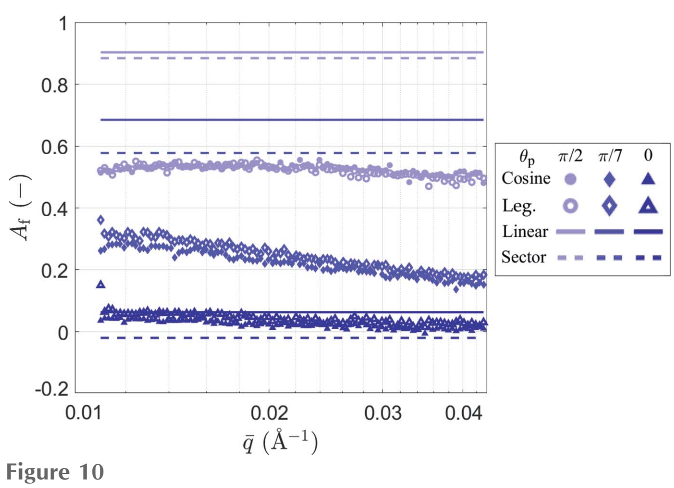

Figure 10
Anisotropy factor $A_{\rm f}$ versus average q value for annular averaging, $\overline{q}$, calculated from the cosine expansion [filled circles, diamonds and triangles; equation (6)], the Legendre expansion [open circles, diamonds and triangles; equation (8)], the axial line integration method [solid lines; equation (9)] and the axial sector integration method [dashed lines; equation (9)] for a CTAB/NaSal WLM solution experiencing a 10 s^{-1} shear rate in the radial configuration (filled and open circles; $\theta_{\rm p} = \pi/2$), the tangential configuration (filled and open triangles; $\theta_{\rm p} = 0$) and an intermediate configuration (filled and open diamonds; $\theta_{\rm p} = \pi/7$).

especially the inclusion of off-axis data. Interestingly, the linear and sector integration methods agree at $\theta_p = \pi/2$ and $\theta_p = 0$ but disagree at $\theta_p = \pi/7$, where linear integration produces a larger anisotropy factor than the sector integration. This is a reversal of the trend observed for the theoretical data [Fig. 9(*a*)], where the linear integration yielded a smaller anisotropy factor than the sector integration.

4. Discussion

Calculation of the anisotropy factor directly from the cylindrical form factor yields different results depending on the method chosen: cosine expansion, Legendre expansion or axial integration. Though all methods estimate an A_f approaching 1 for an infinitesimal rod radius, they disagree at finite rod radii [compare Fig. 6(*b*) with Fig. S3(*b*)]. Specifically, expansion methods do not produce an A_f approaching 1, while integration methods do. The inclusion of intensity data at all ϕ_s when using the expansion methods reduces A_f. Integration methods exclude data away from the scattering axes, resulting in larger anisotropy factor estimates. Data exclusion can make integration methods more challenging to use when faced with certain scattering phenomena, like asymmetry along q_x and q_y. Practitioners must take care not to exclude data that may be necessary for understanding particle morphologies or orientations.

When applied to experimental data, expansion methods produce estimates that agree with each other but not with the axial integration methods (Fig. 10). The anisotropy factors of $\sim$0.5 and $\sim$0.25 from experimental data for $\theta_p = \pi/2$ and $\theta_p = \pi/7$, respectively, at $q = 0.02$ Å^{-1} are well below the A_f values of $\sim$0.9 and $\sim$0.8, respectively, for theoretical data that incorporate non-idealities [Figs. 8(*a*) and 8(*b*)]. This suggests that the experimental data have larger amounts of smearing or, more likely, the WLMs are not aligned as perfectly as the theoretical data. It is also unclear why A_f decreases with $\overline{q}$ at $\theta_p = \pi/7$ in Fig. 10. The expected maximum A_f at $q = j_{1,1}/D = 0.19$ Å^{-1} occurs above the available experimental scattering range examined here. Thus, the negative slope is not a result of using data at q greater than $j_{1,1}/D$. Despite its q dependence, data for $\theta_p = \pi/7$ produce an anisotropy factor smaller than that of $\theta_p = \pi/2$ at all q.

Axial integration yields larger anisotropy factors than the expansion methods for experimental data, where linear integration calculates the largest A_f at all θ_p (Fig. 10). This is the reverse of the relationship between linear and sector integration observed for the theoretical data set, where the linear estimate of A_f was lower than that of the sector integration [Fig. 9(*c*)]. Our experimental WLMs are probably less well aligned than the theoretical rods, resulting in a more isotropic scattering pattern. This causes sector integration to estimate a lower A_f for the experimental data than for the theoretical data.

Fig. 11 illustrates the nonlinear dependence of the anisotropy factor on the rod orientation angle (θ_p) when using theoretical data, where the maximum anisotropy factor at $qL \simeq 1.84L/R$ is reported for the expansion methods. The expansion methods agree with each other at $\theta_p < \pi/8$ but do not agree with the axial methods. At $\theta_p > \pi/8$, all methods agree more closely. Sector axial integration ($\phi_{sect} = 3.15°$) produces the highest estimate of anisotropy factor, while linear axial integration yields the lowest. This is further evidence that each method provides different information about scattering anisotropy and thus material alignment. Fig. 11 also shows that each method has a different dependence on particle tilt. Linear axial integration increases more slowly than the other methods, making it a good candidate for resolving differences in particle orientation angle. Axial sector integration is not sensitive to orientation angles above $\theta_p \simeq \pi/16$. Thus, sectors are useful for identifying the maximal anisotropy but are less sensitive to particle tilt or projected length.

Expansion and axial integration methods do not probe the same aspects of morphology, alignment or orientation. Axial methods are not sensitive to morphological features or q range [compare Fig. 8 with Fig. S3(*b*)] and only consider the most aligned elements of the orientation distribution, depending on sector selection. However, expansion methods consider contributions to scattering from the entire orientation distribution of a particle, but each contribution is weighted differently based on the type of expansion selected (cosine versus Legendre). A practitioner must decide which method for determining the anisotropy factor is best for their analytical goals.

All the anisotropy factor calculation methods examined here evaluate the amount of anisotropy in a scattering pattern and do not directly quantify the alignment within or the polydispersity of a particle suspension. Thus, these methods are anisotropy factors, not alignment factors, which directly describe an orientation distribution. Anisotropy factors can be generalized to many particle morphologies, allowing for comparison between measurements, assuming the same calculation method is chosen for each analysis. These anisotropy factors could then be related to orientation using alignment factors that are specific to a particle morphology,

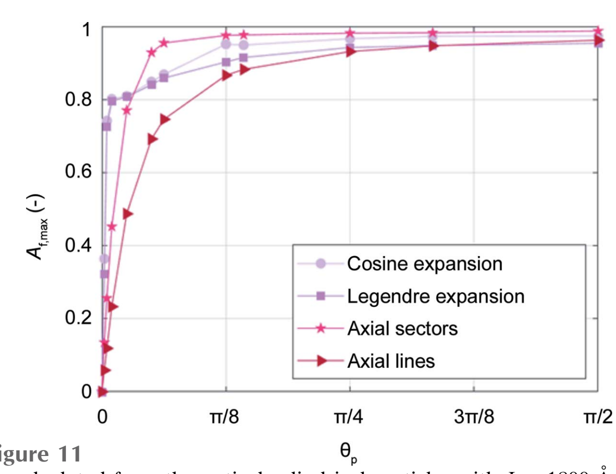

Figure 11
A_f calculated from theoretical cylindrical particles with $L = 1800$ Å and $R = 20$ Å for the examined methods with changing particle orientation θ_p relative to the neutron beam, showing axial lines as the most effective method for resolving particle orientation.

Version of Record at: https://doi.org/10.1107/S1600576723002182

like rods. Separating scattering anisotropy analyses (anisotropy factor) from analyses of particle orientation or alignment (alignment factor) will allow for clearer links to be drawn between anisotropy and alignment.

5. Conclusions

Data selection is the step that most influences anisotropy factor estimates for all methods analyzed here. Our results identify some guidelines for data selection when analyzing 2D SANS data for a suspension of rigid rod-like particles:

(i) Data should generally fall within $2\pi \le qL \le j_{1,1}L/R$.

(ii) Data near $qL = 1.84L/R$ should be included when possible, especially for expansion methods.

(iii) The maximum available q range should be used for annular averaging or integration, while fulfilling guideline (i).

(iv) Sector averages should use sector angles within $\mathrm{FWHM}/10 \le \phi_{\mathrm{sect}} \le \mathrm{FWHM}$.

These guidelines are supplemented by conditions on bin count and annular area [equation (12)] that are detailed in Sections 3.2.2 and 3.2.3 (and Section S2), where a minimum bin count of 20 bins is recommended for annular averaging to generate a representative anisotropy factor. Bin count is particularly important in q ranges near the beam stop, where the small number of data points may influence estimates of the anisotropy factor. Altogether, these provide a framework for selecting data in a standardized way, bringing the anisotropy factor and scattering communities closer to a standardized method for determining the anisotropy factor. It must be emphasized that these are guidelines on how to begin data analysis, not rules that must be followed in all analyses. Further work is needed to generalize these guidelines to other particle morphologies.

Finite detector resolution, smearing effects from a 15% scattering vector spread and particle polydispersity decrease anisotropy factor estimates by approximately 10% (compare Fig. 8 with Fig. 6). These measurement non-idealities must be accounted for when interpreting the anisotropy factor. As this study only considers cylindrical morphologies, other morphologies may require adjusted criteria. A future study exploring a broader set of morphologies would help clarify the guidelines for standardizing the anisotropy factor.

Our experimental example applies each anisotropy factor analysis method to theoretical and experimental data for cylindrical particles. Axial sector integration generates higher anisotropy factor estimates than expansion methods, because axial integration excludes data that do not fall on the axes. This agrees with findings for the theoretically generated data. The experimental results produce lower anisotropy factors than the theoretical results, suggesting that the WLM system is not as well aligned as the perfectly aligned theoretical rods. Future work will examine the effects of polydispersity in the orientation distribution or imperfect alignment on the anisotropy factor.

Axial integration methods only quantify the maximally aligned elements in the scattering pattern. Expansion methods provide a more holistic picture of scattering anisotropy, where scattering from all aspects of the orientation distribution contributes to the calculation. Because these analysis methods are not directly related to alignment or orientation and only consider scattering anisotropy, they should be classified as ‘anisotropy factors’. The term ‘alignment factor’ can then be reserved for more direct analyses of particle orientation. This separation of anisotropy and alignment factors will allow for oriented systems to be easily compared with anisotropy factors, while orientation can be defined using alignment factors for specific morphologies, like rods.

Anisotropy factors are a useful tool for quickly assessing the anisotropy of a 2D scattering pattern and they allow for basic analysis of the alignment in orientable systems. Comparison of anisotropy factor estimates from axial and expansion methods remains a challenge. A process for careful interconversion between anisotropy factor calculation methods would be useful for the anisotropic scattering community. This could be achieved by determining how the anisotropy factor correlates to real particle alignment and orientation. The topic of correlating anisotropy factors to orientation distributions is not broached here, as this work is focused on methods used to calculate anisotropy factor.

Acknowledgements

Certain commercial equipment, instruments, materials, suppliers or software are identified in this paper to foster understanding. Such identification does not imply recommendation or endorsement by the National Institute of Standards and Technology, nor does it imply that the materials or equipment identified are necessarily the best available for the purpose. We are grateful to the ILL for support during data collection and analysis.

Funding information

Support for Jack Rooks was provided via the Summer Undergraduate Research Fellowship (SURF) program that is part of the Center for High Resolution Neutron Scattering (CHRNS), a partnership between the National Institute of Standards and Technology and the National Science Foundation under agreement No. DMR-2010792. This research was performed while Peter Gilbert held an NRC Research Associateship award at the NCNR. This work benefitted from the use of the *SasView* application, originally developed under NSF award DMR-0520547. *SasView* contains code developed with funding from the European Union’s Horizon 2020 research and innovation programme under the SINE2020 project, grant agreement No. 654000.

References

Andriano, L. T., Ruocco, N., Peterson, J. D., Olds, D., Helgeson, M. E., Ntetsikas, K., Hadjichristidis, N., Costanzo, S., Vlassopoulos, D., Hjelm, R. P. & Leal, L. G. (2020). *J. Rheol.* **64**, 663–672.

Chatelain, P. (1955). *Bull. Soc. Minéral. Cristallogr.* **78**, 262–266.

Corona, P. T., Ruocco, N., Weigandt, K. M., Leal, L. G. & Helgeson, M. E. (2018). *Sci. Rep.* **8**, 15559.

Corona, P. T., Silmore, K. S., Adkins, R., Lang, C., Lettinga, M. P., Swan, J. W., Leal, L. G. & Helgeson, M. E. (2021). *Phys. Rev. Mater.* **5**, 065601.

Dewhurst, C. (2003). *GRAS$_{ANS}$P*. Manual Version 2.0. Report No. ILL03DE01T. Institut Laue–Langevin, Grenoble, France. https://www.ill.eu/fileadmin/user_upload/ILL/3_Users/Scientific_groups/Large_Scale_Structures/Grasp/Download/grasp_manual.pdf.

Doucet, M., Cho, J. H., Alina, G., Attala, Z., Bakker, J., Bouwman, W., Butler, P., Campbell, K., Cooper-Benun, T., Durniak, C., Forster, L., Gonzalez, M., Heenan, R., Jackson, A., King, S., Kienzle, P., Krzywon, J., Murphy, R., Nielsen, T., O'Driscoll, L., Potrzebowski, W., Prescott, S., Ferraz Leal, R., Rozyczko, P., Snow, T. & Washington, A. (2021). *SasView*. Version 5.0.4. https://zenodo.org/record/4467703.

Eberle, A. P. R. & Porcar, L. (2012). *Curr. Opin. Colloid Interface Sci.* **17**, 33–43.

Fuller, G. G. (1995). *Optical Rheometry of Complex Fluids*, pp. 63–64. New York: Oxford University Press.

Gazeau, F., Dubois, E., Bacri, J. C., Boué, F., Cebers, A. & Perzynski, R. (2002). *Phys. Rev. E*, **65**, 031403.

Gilbert, P. H. & Giacomin, A. J. (2019). *Phys. Fluids*, **31**, 103104.

Haase, W., Fan, Z. X. & Müller, H. J. (1988). *J. Chem. Phys.* **89**, 3317–3322.

Hammouda, B. (2008). *Probing Nanoscale Structure – The SANS Toolbox*. National Institute of Standards and Technology, Gaithersburg, Maryland, USA. https://web.archive.org/web/20220320085815/https://www.ncnr.nist.gov/staff/hammouda/the_SANS_toolbox.pdf.

Hayward, D. W., Magro, G., Hörmann, A., Prévost, S., Schweins, R., Richardson, R. M. & Gradzielski, M. (2021). *Rev. Sci. Instrum.* **92**, 033903.

Hongladarom, K., Ugaz, V. M., Cinader, D. K., Burghardt, W. R., Quintana, J. P., Hsiao, B. S., Dadmun, M. D., Hamilton, W. A. & Butler, P. D. (1996). *Macromolecules*, **29**, 5346–5355.

Iwase, H., Kawai, R., Morishima, K., Takata, S. I., Yoshimura, T. & Shibayama, M. (2019). *J. Colloid Interface Sci.* **538**, 357–366.

Jeffries, C. M., Ilavsky, J., Martel, A., Hinrichs, S., Meyer, A., Pedersen, J. S., Sokolova, A. V. & Svergun, D. I. (2021). *Nat. Rev. Methods Primers*, **1**, 70.

Krzywon, J. (2014). *Anton Paar MCR-501 Rheometer*, https://www.ncnr.nist.gov/programs/sans/equipment/rheometer.html.

Kurta, R. P., Wiegart, L., Fluerasu, A. & Madsen, A. (2019). *IUCrJ*, **6**, 635–648.

Lacková, V., Schroer, M. A., Honecker, D., Hähsler, M., Vargová, H., Zakutanská, K., Behrens, S., Kováč, J., Svergun, D. I., Kopčanský, P. & Tomašovičová, N. (2021). *iScience*, **24**, 103493.

Lemaire, B. J., Davidson, P., Ferré, J., Jamet, J. P., Petermann, D., Panine, P., Dozov, I. & Jolivet, J. P. (2004). *Eur. Phys. J. E*, **13**, 291–308.

Liberatore, M. W., Nettesheim, F., Vasquez, P. A., Helgeson, M. E., Wagner, N. J., Kaler, E. W., Cook, L. P., Porcar, L. & Hu, Y. T. (2009). *J. Rheol.* **53**, 441–458.

Liebi, M., van Rhee, P. G., Christianen, P. C., Kohlbrecher, J., Fischer, P., Walde, P. & Windhab, E. J. (2013). *Langmuir*, **29**, 3457–3473.

Lovell, R. & Mitchell, G. R. (1981). *Acta Cryst.* A**37**, 135–137.

Maier, W. & Saupe, A. (1959). *Z. Naturforsch. Teil A*, **14**, 882–889.

Markmann, V., Dartsch, M., Valerio, J., Frenzel, L., Lokteva, I., Walther, M., Westermeier, F., Grübel, G. & Lehmkühler, F. (2020). *Struct. Dyn.* **7**, 054901.

Muthig, M., Prévost, S., Orglmeister, R. & Gradzielski, M. (2013). *J. Appl. Cryst.* **46**, 1187–1195.

Porcar, L. & Gilbert, P. (2021). *RheoSANS Investigation of Wormlike Micelle Orientation*, https://doi.ill.fr/10.5291/ILL-DATA.EASY-1063. Institut Laue–Langevin, Grenoble, France.

Pujari, S., Dougherty, L., Mobuchon, C., Carreau, P. J., Heuzey, M. C. & Burghardt, W. R. (2011). *Rheol. Acta*, **50**, 3–16.

Richards, J. J. & Riley, J. K. (2019). *Curr. Opin. Colloid Interface Sci.* **42**, 110–120.

Rosén, T., Brouzet, C., Roth, S. V., Lundell, F. & Söderberg, L. D. (2018). *J. Phys. Chem. C*, **122**, 6889–6899.

Salem, A. J. & Fuller, G. G. (1985). *J. Colloid Interface Sci.* **108**, 149–157.

Schmidt, G., Nakatani, A. I., Butler, P. D. & Han, C. C. (2002). *Macromolecules*, **35**, 4725–4732.

Sivia, D. S. (2011). *The Basics of X-ray and Neutron Scattering. Elementary Scattering Theory*, pp. 63–92. New York: Oxford University Press.

Wade, M. A., Walsh, D., Lee, J. C. W., Kelley, E., Weigandt, K., Guironnet, D. & Rogers, S. A. (2020). *Soft Matter*, **16**, 4899–5096.

Walker, L. M. (1995). PhD thesis, University of Delaware, USA.

Walker, L. M. & Wagner, N. J. (1996). *Macromolecules*, **29**, 2298–2301.

Wang, Z., Lam, C. N., Chen, W.-R., Wang, W., Liu, J., Liu, Y., Porcar, L., Stanley, C. B., Zhao, Z., Hong, K. & Wang, Y. (2017). *Phys. Rev. X*, **7**, 031003.

Zaluzhnyy, I. A., Kurta, R. P., Scheele, M., Schreiber, F., Ostrovskii, B. I. & Vartanyants, I. A. (2019). *Materials*, **12**, 3464.